

Environmentally Assisted Cracking in Light Water Reactors

Annual Report
January—December 2003

Manuscript Completed: May 2005
Date Published: May 2006

Prepared by
B. Alexandreanu, O. K. Chopra, H. M. Chung, E. E. Gruber,
W. K. Soppet, R. W. Strain, and W. J. Shack

Argonne National Laboratory
9700 South Cass Avenue
Argonne, IL 60439

W. H. Cullen, Jr., and C. E. Moyer, NRC Project Managers

Prepared for
Division of Fuel, Engineering & Radiological Research
Office of Nuclear Regulatory Research
U.S. Nuclear Regulatory Commission
Washington, DC 20555-0001
NRC Job Code Y6388



Previous Documents in Series

Environmentally Assisted Cracking in Light Water Reactors Semiannual Report

- April—September 1985*, NUREG/CR-4667 Vol. I, ANL-86-31 (June 1986).
October 1985—March 1986, NUREG/CR-4667 Vol. II, ANL-86-37 (September 1987).
April—September 1986, NUREG/CR-4667 Vol. III, ANL-87-37 (September 1987).
October 1986—March 1987, NUREG/CR-4667 Vol. IV, ANL-87-41 (December 1987).
April—September 1987, NUREG/CR-4667 Vol. V, ANL-88-32 (June 1988).
October 1987—March 1988, NUREG/CR-4667 Vol. 6, ANL-89/10 (August 1989).
April—September 1988, NUREG/CR-4667 Vol. 7, ANL-89/40 (March 1990).
October 1988—March 1989, NUREG/CR-4667 Vol. 8, ANL-90/4 (June 1990).
April—September 1989, NUREG/CR-4667 Vol. 9, ANL-90/48 (March 1991).
October 1989—March 1990, NUREG/CR-4667 Vol. 10, ANL-91/5 (March 1991).
April—September 1990, NUREG/CR-4667 Vol. 11, ANL-91/9 (May 1991).
October 1990—March 1991, NUREG/CR-4667 Vol. 12, ANL-91/24 (August 1991).
April—September 1991, NUREG/CR-4667 Vol. 13, ANL-92/6 (March 1992).
October 1991—March 1992, NUREG/CR-4667 Vol. 14, ANL-92/30 (August 1992).
April—September 1992, NUREG/CR-4667 Vol. 15, ANL-93/2 (June 1993).
October 1992—March 1993, NUREG/CR-4667 Vol. 16, ANL-93/27 (September 1993).
April—September 1993, NUREG/CR-4667 Vol. 17, ANL-94/26 (June 1994).
October 1993—March 1994, NUREG/CR-4667 Vol. 18, ANL-95/2 (March 1995).
April—September 1994, NUREG/CR-4667 Vol. 19, ANL-95/25 (September 1995).
October 1994—March 1995, NUREG/CR-4667 Vol. 20, ANL-95/41 (January 1996).
April—December 1995, NUREG/CR-4667 Vol. 21, ANL-96/1 (July 1996).
January 1996—June 1996, NUREG/CR-4667 Vol. 22, ANL-97/9 (June 1997).
July 1996—December 1996, NUREG/CR-4667 Vol. 23, ANL-97/10 (October 1997).
January 1997—June 1997, NUREG/CR-4667 Vol. 24, ANL-98/6 (April 1998).
July 1997—December 1997, NUREG/CR-4667 Vol. 25, ANL-98/18 (September 1998).
January 1998—June 1998, NUREG/CR-4667 Vol. 26, ANL-98/30 (December 1998).
July 1998—December 1998, NUREG/CR-4667 Vol. 27, ANL-99/11 (October 1999).
January 1999—June 1999, NUREG/CR-4667 Vol. 28, ANL-00/7 (July 2000).
July 1999—December 1999, NUREG/CR-4667 Vol. 29, ANL-00/23 (November 2000).
January 2000—June 2000, NUREG/CR-4667 Vol. 30, ANL-01/08 (June 2001).
July 200—December 2000, NUREG/CR-4667 Vol. 31, ANL-01/09 (April 2002).

Environmentally Assisted Cracking in Light Water Reactors Annual Report

- January—December 2001*, NUREG/CR-4667 Vol. 32, ANL-02/33 (June 2003).
January—December 2002, NUREG/CR-4667 Vol. 33, ANL-03/36 ().

Abstract

This report summarizes work performed by Argonne National Laboratory on fatigue and environmentally assisted cracking (EAC) in light water reactors (LWRs) from January to December 2003. Topics that have been investigated include: (a) environmental effects on fatigue crack initiation in carbon and low-alloy steels and austenitic stainless steels (SSs), (b) irradiation-assisted stress corrosion cracking (IASCC) of austenitic SSs in boiling water reactors (BWRs), (c) evaluation of causes and mechanisms of irradiation-assisted cracking of austenitic SS in pressurized water reactors (PWRs), and (d) cracking in Ni alloys and welds.

Fatigue tests have been conducted on two heats of Type 304 stainless steel (SS) under various material conditions to determine the effect of heat treatment on fatigue crack initiation in these steels in air and LWR environments. Heat treatment has little or no effect on the fatigue life in air and low dissolved oxygen (DO) environment, whereas in a high-DO environment, fatigue life is lower for sensitized SSs.

Crack growth rate (CGR) data were obtained on Type 304L SS (Heat C3) irradiated to 0.3×10^{21} n/cm², nonirradiated Type 304 L SS submerged-arc weld heat affected zone (HAZ) specimens from the Grand Gulf (GG) reactor core shroud, and a Type 304 SS laboratory-prepared shielded metal arc weld. The irradiated specimen of Heat C3 showed very little enhancement of CGRs in high-DO water. The results for the weld HAZ material indicate that under predominantly mechanical fatigue conditions, the CGRs for the GG Type 304L weld HAZ are lower than those for shielded metal arc (SMA) weld HAZ prepared in the laboratory with Type 304 SS.

Slow-strain-rate tensile (SSRT) tests have been completed in high-purity 289°C water on steels irradiated to ≈ 3 dpa. The bulk sulfur (S) content correlated well with the susceptibility to intergranular stress corrosion cracking (IGSCC) in 289°C water. The irradiation-assisted stress corrosion cracking (IASCC) susceptibility of SSs that contain >0.003 wt.% S increased drastically. These results and a review of other data in the literature indicate that IASCC in 289°C water is dominated by a crack-tip grain-boundary process that involves S. The IASCC-resistant or susceptible behavior of austenitic SSs in BWR-like oxidizing environment is described in terms of a two-dimensional map of bulk S and carbon (C) contents of the steels.

Crack growth tests were completed on a Alloy 600 round robin specimen and a Alloy 182 weld specimen in simulated PWR water at 320°C. Under cyclic loading, the CGRs for the weld specimen were a factor of ≈ 5 higher than those for Alloy 600 under the same loading conditions in air; little or no environmental enhancement was observed. The CGRs obtained with a trapezoidal waveform (i.e., a constant load with periodic unload/reload) were comparable to the average behavior of Alloy 600 in a PWR environment. The cyclic CGRs for the Alloy 600 round-robin specimen show significant environmental enhancement. However, the crack front was U-shaped, indicating that the growth rates were significantly higher near the edge of the specimen than the center.

Intentionally Left Blank

Foreword

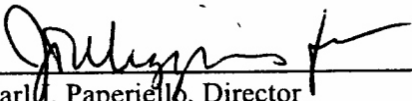
For more than 34 years, Argonne National Laboratory (ANL) has served the U.S. Nuclear Regulatory Commission (NRC), Office of Nuclear Regulatory Research (RES), as a prime contractor for studies of the environmental degradation of structural materials in light-water reactor environments. As Volume 34 in the NUREG/CR-4667 series, this document represents the annual report of ANL program studies for Calendar Year 2003. During this year, the program has evolved to keep pace with the most critical contemporary issues facing the industry and the NRC:

- Task 1 focuses on the environmental degradation of fatigue life of pressure boundary materials.
- Task 2 addresses irradiation-assisted stress corrosion cracking (IASCC) of stainless steels in boiling-water reactor (BWR) environments, while the parallel program in Task 3 addresses IASCC of stainless steels in pressurized-water reactor (PWR) environments.
- Task 4, the study of crack growth rates in nickel-base alloys typically used in vessel penetrations, is currently focused on testing Alloy 600 and its associated weld metals, Alloys 82 and 182.

Studies of the degradation of fatigue life of pressure boundary materials focused on the effects of heat treatment and the degree of sensitization of stainless steels. Sensitization appears to have little or no effect in air or low-dissolved oxygen (i.e., PWR-type environments), and the fatigue life of sensitized stainless steels is lower in high-dissolved oxygen (i.e., BWR-type environments). Moreover, the amount of degradation is linked to the degree of sensitization. In addition, studies of the morphology of incipient fatigue cracks show that fatigue cracks propagate in a transgranular mode in air and PWR-type environments. However, cracks in sensitized stainless steels begin as intergranular cracks, transitioning to transgranular cracks after about 200 mm.

The evaluation of the effects of irradiation on mechanical properties, stress corrosion cracking, and fracture toughness of stainless steels and nickel-base alloys used in reactor core internal structures is an important aspect of the ANL program. The database of IASCC results was extended this year, reinforcing the previous conclusion that IASCC degradation is directly linked to sulfur content of the steels. However, extremely low sulfur, coupled with very low carbon content (i.e., very clean steel), also creates susceptibility to IASCC. Crack growth rate testing of Type 304 and Type 304L stainless steel aimed to establish the threshold for IASCC as functions of water chemistry and irradiation damage. Future IASCC work will test materials that have received higher radiation doses, and will involve more microstructural characterization of such materials.

Evaluation of the stress corrosion crack growth resistance of nickel-base alloys continued during this period, and will continue for the foreseeable future. Crack growth rate tests on Alloy 182 weld metal indicate that growth rates are about a factor of five greater than those for Alloy 600 under the same test conditions. In future years, the stress corrosion crack studies of nickel-base alloys will begin to focus more on Alloy 690 and its associated weld metal, Alloy 152, including cold-worked and heat-affected zone forms of the wrought material.



Carlo J. Paperiello, Director
Office of Nuclear Regulatory Research
U.S. Nuclear Regulatory Commission

Intentionally Left Blank

Contents

Abstract.....	iii
Foreword	v
Executive Summary.....	xvii
Acknowledgments	xix
Abbreviations.....	xxi
1 Introduction	1
2 Environmental Effects on Fatigue Crack Initiation in Carbon and Low-Alloy Steels and Austenitic Stainless Steels.....	3
2.1 Introduction.....	3
2.2 Experimental	4
2.3 Results – Effect of Heat Treatment on Fatigue Life.....	7
2.3.1 Fatigue ϵ -N Behavior.....	7
2.3.2 Fatigue Crack and Fracture Surface Morphology	10
3 Irradiation-Assisted Stress Corrosion Cracking of Austenitic Stainless Steel in BWRs.....	23
3.1 Slow-Strain-Rate-Tensile Test of Model Austenitic Stainless Steels Irradiated in the Halden Reactor.....	23
3.1.1 Introduction.....	23
3.1.2 Representation of IASCC-Resistant or –Susceptible Behavior of 304- and 316-Type Steels in Sulfur-Carbon Map.....	24
3.1.3 Grain-Boundary Segregation of Sulfur and Carbon.....	26
3.1.4 Analysis of Solubility of Carbon in Sulfides	30
3.2 Crack Growth Rate Test of Austenitic Stainless Steels Irradiated in the Halden Reactor.....	32
3.2.1 Introduction.....	32
3.2.2 Experimental	33
3.2.2.1 Specimen Geometry and Materials	33
3.2.2.2 Test Procedure.....	38
3.2.3 Crack Growth Rates of Irradiated Stainless Steels in BWR Environments	41

3.2.3.1	Specimen C3–A of Type 304L SS, Test CGRI-12	41
3.2.3.2	Irradiated Austenitic SSs under Continuous Cycling	44
3.2.3.3	CGRs of Irradiated Austenitic SSs under Trapezoidal Waveform with Long Hold Periods	45
3.2.4	Crack Growth Tests on Nonirradiated Stainless Steel Weld HAZ Specimens	46
3.2.4.1	Specimen GG5B–A of the HAZ from Grand Gulf Core Shroud H5 SA Weld, Test CGR–10	46
3.2.4.2	Specimen 85–3A–TT of the HAZ from Laboratory–Prepared SMA Weld, Test CGR-11	49
3.2.4.3	Specimen GG3B–A–TT of the HAZ from Grand Gulf Core Shroud H5 SA Weld, Test CGR-14.....	56
3.2.4.4	Austenitic SS Weld HAZ under Continuous Cycling.....	59
3.2.4.5	Austenitic SS Weld HAZ under Constant Load or Cycling with Long Hold Periods.....	61
4	Evaluation of Causes and Mechanisms of Irradiation-Assisted Cracking of Austenitic Stainless Steel in PWRs.....	63
4.1	Introduction.....	63
4.2	Irradiation of Austenitic Stainless Steels in the BOR-60 Reactor	63
4.3	Representation of IASCC–Resistant or –Susceptible Behavior of Types 304 and 316 Stainless Steel in Sulfur–Carbon Map	64
5	Cracking of Nickel Alloys and Welds	67
5.1	Introduction.....	67
5.2	Experimental	68
5.2.1	Material and Specimen Design.....	68
5.2.2	Test Facility	70
5.2.3	Test Procedure	70
5.2.4	Material Characterization.....	71
5.2.4.1	Alloy 600 for the Round Robin Specimen	71
5.2.4.2	Double–J Weld.....	74
5.3	Results	85

5.3.1	Alloy 600 Round Robin Specimen.....	85
5.3.2	Alloy 182 Double-J Weld Specimen.....	90
6	Summary.....	99
6.1	Environmental Effects on Fatigue ϵ -N Behavior.....	99
6.2	Irradiation-Assisted Stress Corrosion Cracking of Austenitic Stainless Steel in BWRs ..	99
6.3	Irradiation-Assisted Cracking of Austenitic Stainless Steel in PWRs.....	100
6.4	Cracking of Nickel Alloys and Welds.....	101
	References.....	103

Figures

1. Typical microstructures observed by SEM, showing degree of sensitization for alloys used in this study.	5
2. Configuration of fatigue test specimen.....	6
3. Schematic diagram of electron–beam–welded bar for machining A302–Gr B fatigue test specimens.	6
4. Effect of material heat treatment on fatigue life of Type 304 stainless steel in air, BWR, and PWR environments at 289°C, ≈0.38% strain amplitude, sawtooth waveform, and 0.004%/s tensile strain rate.	8
5. Effect of sensitization annealing on fatigue life of Type 304 and 316 stainless steel in low–DO water at 325°C.....	8
6. Effect of sensitization anneal on the fatigue lives of Type 304 and 316NG stainless steel in high–DO water.	9
7. Cyclic stress response of Heat 30956: MA, MA + 0.67 h at 700°C, and MA + 24 h at 700°C; and Heat 10285, MA + 24 h at 600°C in air, BWR, and PWR environments at 289°C.....	9
8. Photomicrographs showing sites of crack initiation on fracture surfaces of Type 304 SS specimens tested in air.....	11
9. Photomicrographs showing sites of crack initiation on fracture surfaces of Type 304 SS specimens tested in simulated BWR environment.....	13
10. Photomicrographs showing the sites of crack initiation on the fracture surfaces of Type 304 SS specimen tested in simulated PWR environment.	14
11. Low– and high–magnification photomicrographs showing striations at select locations on fracture surfaces of MA specimen of Heat 30956 in simulated BWR environment.	14
12. Photomicrographs showing striations at select locations on fracture surfaces of MA specimens of Heat 30956 heat–treated for 0.67 h at 700°C in air, BWR, and PWR environments.	15
13. Photomicrographs showing striations at select locations on fracture surfaces of MA specimens of Heat 10285 heat–treated for 24 h at 600°C in air, BWR, and PWR environments.	16
14. Photomicrographs showing striations at select locations on fracture surfaces of MA specimens of Heat 30956 heat–treated for 24 h at 700°C in air, BWR, and PWR environments.	17
15. Photomicrographs of the crack morphology of Type 304 SS under all test and environmental conditions.	18
16. Photomicrographs showing crack initiation site at low and high magnification, and striations at select locations in Type 316NG SS tested in air.....	19

17. Photomicrographs showing crack initiation site and striations at select locations in Type 316NG SS tested in BWR and PWR environment.	20
18. Photomicrographs showing the morphology of lateral cracks formed in Type 316NG SS in three test environments.	21
19. Range of bulk S and C contents in which 304- or 316-type steels are resistant or susceptible to IASCC in BWR-like oxidizing water.	25
20. Expanded view of low-S portion of Fig. 19 showing data in detail.	25
21. Range of bulk S and C contents in which 304- or 316-type steels are resistant or susceptible to IASCC, including four susceptible heats tested at 1.3 dpa in this study.	26
22. High-magnification fractograph of H-charged BWR neutron absorber tube, 304 SS, Heat B, ≈ 3 dpa; fracture was produced at 23°C in ultra-high vacuum environment in a scanning Auger electron microscope.	27
23. Summary of AES analysis of grain-boundary segregation of S and C in BWR neutron absorber tube fabricated from Type 304 SS Heat A and irradiated to 3 dpa: S and C peak heights from ductile and IG fracture surfaces are compared.	28
24. Summary of AES analysis of grain-boundary segregation of S and C in BWR neutron absorber tube fabricated from Type 304 SS Heat B and irradiated to 3 dpa: S and C peak heights from ductile and IG fracture surfaces are compared.	28
25. Result of AES depth-profiling analysis of grain-boundary segregation of S and C in BWR neutron absorber tubes fabricated from Type 304 SS Heats A and B and irradiated to ≈ 3 dpa.	29
26. AES signal showing high concentrations of Cu, S, and C in CuS-type precipitate denoted with number “6” in Fig. 22.	30
27. AES signal showing a high concentration of C in CuS-type precipitate in BWR neutron absorber tube, 304 SS, Heat B, ≈ 3 dpa.	31
28. AES signal showing a high concentration of C in another CuS-type precipitate in BWR neutron absorber tube, 304 SS, Heat B, ≈ 3 dpa.	31
29. Configuration of compact-tension specimen for this study.	33
30. Orientation of the 1/4-T CT specimens from the Grand Gulf H5 SA weld HAZ and laboratory-prepared SMA weld HAZ.	34
31. Low- and high-magnification photomicrographs of the structure of the Type 304L base metal from the top shell of the H5 weld of the Grand Gulf core shroud.	35
32. Micrographs of the interface between the weld metal and top shell of the H5 weld of the Grand Gulf core shroud.	35
33. Low- and high-magnification photomicrographs of the structure of the Type 304L base metal from the bottom shell of the H5 weld of the Grand Gulf core shroud.	36

34. Micrographs of the interface between the weld metal and bottom shell of the H5 weld of the Grand Gulf core shroud.	36
35. Low- and high-magnification photomicrographs of the structure of Heat 10285 of the Type 304 base metal from the top shell of the H5 weld of the Grand Gulf core shroud.	37
36. Micrographs of the interface between the weld metal and base metal.	37
37. Plot of CGR in water vs. the CGR in air showing environmental enhancement of growth rates in high purity water at 289°C.	40
38. Crack length vs. time plots for irradiated Type 316 SS in high-purity water at 289°C during test periods 1-2, 3-5, 6-7, 8-10, and 11-12.	42
39. Photomicrograph of the fracture surface of Specimen C3-A.	44
40. CGR data for irradiated austenitic SSs under continuous cycling at 289°C in high-purity water with ≈ 300 ppb and < 30 ppb dissolved oxygen.	44
41. CGR data under constant load with periodic partial unloads for irradiated austenitic SSs in high-purity water at 289°C.	45
42. Crack length vs. time plots for nonirradiated HAZ specimen of Grand Gulf Type 304L bottom shell H5 weld in high-purity water at 289°C during test periods precracking-3, 4-6, and 7-8.	47
43. Photomicrograph of the fracture surface of Specimen GG5B-A.	48
44. Micrograph of the fracture surface of Specimen GG5B-A tested in high-DO water at 289°C.	48
45. Micrographs showing slice of the entire length of fracture surface, and high magnification micrographs of the fracture surface at locations 1, 2, and 3, respectively.	49
46. Change in crack length and ECP of Pt and SS electrodes during test periods 5-6 and the intermediate transition period.	50
47. Photomicrographs of the fracture surfaces of the two halves of Specimen 85-3A-TT.	51
48. Micrograph of the cross section of Specimen 85-3A-TT showing the fracture plane profile.	51
49. Crack length vs. time plots for nonirradiated HAZ specimen of Grand Gulf Type 304L bottom shell H5 weld HAZ in high-purity water at 289°C during test periods 1-3, 4-6, 7-8, and 9.	52
50. Micrograph of the fracture surface of Specimen 85-3A-TT tested in high-DO water at 289°C.	53
51. Micrograph showing slice of the fracture surface that was perpendicular to the stress axis, and high-magnification micrographs of the fracture surface at locations 1, 2, and 3, respectively.	54
52. Typical fracture morphologies along the change in the fracture plane direction and before and after the change in direction.	55

53. Micrograph of the cross section of Specimen GG3B-A-TT showing the fracture plane profile.....	57
54. Micrograph of the fracture surface of Specimen GG3B-A-TT tested in high-DO water at 289°C.....	57
55. Crack length vs. time plots for nonirradiated thermally treated Type 304L bottom shell HAZ from the Grand Gulf H5 SA weld in high-purity water at 289°C during test periods precracking, 1-5, and 5-7.	58
56. Micrographs showing slice of the entire length of the fracture surface and high-magnification micrographs of the fracture surface at locations 1, 2, and 3, respectively.	59
57. CGR data for nonirradiated specimens of laboratory-prepared Type 304 SS SMA weld HAZ and Type 304L SA weld HAZ from the Grand Gulf core shroud under continuous cycling at 289°C in high-purity water with 300-500 ppb dissolved oxygen.....	60
58. CGR data under constant load with or without periodic partial unloads for nonirradiated SS weld HAZ specimens in high-purity water at 289°C.....	61
59. Representation of IASCC resistance or susceptibility of austenitic stainless steels as function of bulk S and C contents. Data obtained from PWR- or VVER-irradiated specimens in PWR, VVER, or PWR-like water reported in 1987-2004.	64
60. Configuration of compact-tension specimen used for this study.....	69
61. Schematic of the weld joint design and weld passes.	69
62. Orientation of the CT specimen from the Alloy 182 SMA weld.....	70
63. Microstructure of the round robin Alloy 600 etched with nital and phosphoric acid solution.	72
64. Microstructure of the round robin alloy in the plane of the crack at two magnifications.	73
65. Microstructure of the round robin alloy in the plane of the crack at two magnifications and that of a different heat of Alloy 600, used previously in our experiments.....	73
66. Schematic showing the locations of the three samples cut from the weld.....	74
67. (a) Weld microstructure from Sample 1; transition area between the weld and Alloy 600; and dendritic microstructure in the weld.....	75
68. Large grain microstructure in the HAZ at two opposite positions.....	76
69. Dendritic microstructure on sample 3A, and at a weld pass.	76
70. Examples of dendritic microstructure at a weld passes on sample 3B and high magnification micrographs at the respective locations.....	77
71. Dendritic microstructure on sample 3B and high magnification of a region.	77
72. Dendritic microstructure observed on the surface of sample 3A at 100× and 200× magnifications.	78

73. Micrograph showing one of the matrix precipitates observed on the surface of sample 3A and EDX spectra resulting from the bulk and the precipitate.	78
74. Micrographs showing the microstructure on plane 3A, and matrix and grain boundary precipitates, and EDX spectra resulting from the bulk and from the grain boundary precipitate.	79
75. Micrographs showing Ti-rich precipitates in the weld material, and maps showing the topography at the locations where the high magnification micrographs were taken.	80
76. Micrographs showing the heat affected zone, and high magnification micrographs showing precipitates in the heat affected zone.	81
77. OIM map of the weld, on plane “B”, sample 3B; the same OIM map showing the orientation of each grain; and legends for crystal directions and the resulting grain boundary character distribution.	82
78. OIM map on the surface of sample 3B and the resulting grain boundary character distribution.	83
79. The same OIM map as in Fig. 78a showing crystal directions and SEM micrograph illustrating the dendritic microstructure of the weld.	84
80. Crack length vs. time plot for Alloy 600 round-robin specimen RR-1 in simulated PWR environment at 320°C during periods 1-5, 3B-5C, 6-7, and 6C-7C.	86
81. CGR data for specimen RR-1 of the Alloy 600 round-robin test in simulated PWR environment at 320°C.	87
82. Entire crack surface of Alloy 600 round robin specimen RR-1 tested in PWR water at 320°C.	88
83. Entire crack surface of Alloy 600 round robin specimen RR-3 tested in PWR water at 320°C.	88
84. Selected portion of the crack surface of Alloy 600 round robin specimen RR-1 tested in PWR water at 320°C showing the changes in fracture morphology, and micrographs taken at the boxed positions 1 and 2.	89
85. Crack length vs. time plot for Alloy 182 SMA weld–metal specimen in simulated PWR environment at 320°C during test periods 1–4a, 4b-5, 6-8, 9, and 10.	91
86. Photomicrograph of the fracture surface of specimen CT31-W01.	92
87. A higher magnification photomicrograph showing entire crack extension in a region in the center of the specimen.	93
88. Transition from TG to IG fracture and higher magnification micrograph of the boxed area showing the tip of a few cracks.	94
89. Mixed TG and IG fracture modes, high magnification micrograph of the boxed area, and micrographs showing the crack tips at locations “1” and “2.”	95

90. Photomicrographs detailing the fracture in a region during test periods with a hold time and/or a high rise time, and high magnification micrographs of positions indicated by arrows.	96
91. Photomicrographs detailing the fracture in a region during test periods with a hold time and/or a high rise time, and high magnification micrographs.....	96
92. CGR data for Alloy 182 SMA weld–metal specimen in simulated PWR environment at 320°C.	97
93. Comparison of the SCC growth rate for the Argonne Alloy 182 weld with the available data for Alloy 182 and 82 welds in simulated PWR environment.	98

Tables

1. Composition of austenitic stainless steels for fatigue tests.	4
2. Fatigue test results for Type 304 stainless steel in air and simulated BWR and PWR environments at 289°C.	7
3. Composition of Heat C3 of Type 304L stainless steel irradiated in the Halden reactor.	33
4. Tensile properties of irradiated Heat C3 of Type 304L stainless steel at 288°C.	33
5. Composition of Type 304 stainless steels investigated.	34
6. Tensile properties of the austenitic stainless steels irradiated in the Halden reactor.	38
7. Crack growth results for Specimen C3-A of Type 304 SS ^a in high-purity water at 289°C.	41
8. Crack growth results for Specimen GG5B-A of Type 304L HAZ in high-purity water at 289°C.	46
9. Crack growth results for Specimen 85-3A-TT of nonirradiated Type 304 SS SMA weld HAZ in high-purity water at 289°C.	50
10. Crack growth results for Specimen GG3B-A-TT of Type 304L HAZ in high-purity water at 289°C.	56
11. Chemical composition of Alloy 600 base metal and Inconel 182 and 82 weld metals.	69
12. Welding process and conditions for various weld passes.	69
13. Chemical compositions of the bulk material and matrix precipitate resulting from EDX analysis.	79
14. Chemical compositions of the bulk material and grain boundary precipitate resulting from EDX analysis.	80
15. Loading conditions for the Alloy 600 round-robin test.	85
16. Crack growth results for Alloy 600 round robin specimen RR-1 in PWR water at 320°C.	85
17. Crack growth data for specimen CT31-W01 TS of Alloy 182 SMA weld in PWR water at 320°C.	90

Executive Summary

The existing fatigue strain vs. life (ϵ - N) data indicate potentially significant effects of light water reactor (LWR) coolant environments on the fatigue resistance of carbon and low-alloy steels, as well as of austenitic stainless steels (SSs). For austenitic SSs, the fatigue lives in LWR environments depend on applied strain amplitude, strain rate, temperature, and dissolved oxygen (DO) in water. A minimum threshold strain is required to cause an environmentally assisted decrease in the fatigue life; strain rate and temperature have a strong effect on fatigue life in LWR environments. Limited data indicate that, the effect of DO on fatigue life may depend on the composition and heat treatment of the steel.

During the present reporting period, fatigue tests have been conducted on two heats of Type 304 SS to determine the effect of heat treatment on fatigue crack initiation in these steels in air and LWR environments. The results indicate that heat treatment has little or no effect on the fatigue life of Type 304 SS in air and low-DO pressurized water reactor (PWR) environment. In a high-DO boiling water reactor (BWR) environment, fatigue life is lower for sensitized SSs; life continues to decrease as the degree of sensitization is increased. The cyclic strain-hardening behavior of Type 304 SS under various heat treatment conditions is identical; only the fatigue life varies in different environments.

In air, irrespective of the degree of sensitization, the fracture mode for crack initiation and crack propagation is transgranular (TG). In the BWR environment, the initial crack appeared intergranular (IG) for all heat-treatment conditions, implying a weakening of the grain boundaries. For all conditions tested, the initial IG mode transformed within 200 μm into a TG mode with cleavage-like features. However, the size of the IG portion of the crack surface increased with the degree of sensitization. By contrast, for all of the samples tested in PWR environments, the cracks initiated and propagated in a TG mode irrespective of the degree of sensitization.

The susceptibility of austenitic SSs and their welds to irradiation-assisted stress corrosion cracking (IASCC) as a function of the fluence level, water chemistry, material chemistry, and fabrication history is being evaluated. Crack growth rate (CGR) tests and slow strain rate tests (SSRTs) are being conducted on model SSs, irradiated at $\approx 288^\circ\text{C}$ in a helium environment in the Halden boiling heavy water reactor. Crack growth tests are also being conducted on irradiated specimens of Type 304 and 304L SS weld heat-affected zone (HAZ) to establish the effects of fluence level on IASCC of these materials.

Slow-strain-rate tensile tests have been completed in high-purity 289°C water on steels irradiated to ≈ 0.43 , 1.3, and 3.0 dpa. The bulk S content provided the only good correlation with the susceptibility to IGSCC in 289°C water. Good resistance to IASCC was observed in Type 304 and 316 steels that contain sulfur concentrations of ≈ 0.002 wt.% or less. The IASCC susceptibility of Type 304, 304L, 316, and 316L steels that contain >0.003 wt.% S increased drastically. Steels containing ≥ 0.008 wt.% were very susceptible at high fluence. A comparison of the results with data available in the literature is presented. The IASCC-resistant or -susceptible behavior of austenitic SSs in a BWR-like oxidizing environment is represented in terms of a two-dimensional map of bulk S and C contents of the steels. To investigate the importance of the roles of S and C on IASCC, evidence of grain-boundary segregation was characterized by Auger electron spectroscopy on BWR neutron absorber tubes fabricated from two heats of Type 304 SS.

Also, CGR data were obtained on Type 304L SS (Heat C3) irradiated to 0.3×10^{21} n/cm^2 (0.45 dpa), nonirradiated Type 304L SS weld HAZ specimens from the Grand Gulf (GG) reactor core shroud and a Type 304 SS laboratory-prepared weld. The irradiated specimen of Heat C3 showed very

little enhancement of CGRs in high-DO water. Under cyclic loading, the CGRs may be represented by the Shack/Kassner model for nonirradiated austenitic SSs in high-purity water with 0.2 ppm DO. Under constant load, the CGRs were below the NUREG-0313 disposition curve for sensitized SSs.

The results for the weld HAZ material indicate that, under predominantly mechanical fatigue loading, experimental CGRs for the GG Type 304L weld HAZ are lower than those for the Type 304 SMA weld HAZ. The CGRs for the Type 304 weld HAZ are consistent, and those for the Type 304 L weld HAZ are a factor of ≈ 2 lower than those predicted for austenitic SSs in air. In the high-DO BWR environment, the cyclic CGRs of Type 304 SS SMA weld HAZ are comparable to those of the GG Type 304L SA weld HAZ. Under constant load, the CGRs of as-welded and as-welded plus thermally treated GG weld HAZ are comparable. For both conditions, the CGRs are a factor of ≈ 2 lower than the NUREG-0313 curve for sensitized SSs in water with 8 ppm DO.

A comprehensive irradiation experiment in the BOR-60 Reactor is in progress to obtain a large number of tensile and disk specimens irradiated under PWR-like conditions at $\approx 325^\circ\text{C}$ to 5, 10, and 40 dpa. Irradiation to ≈ 5 and ≈ 10 dpa has been completed; the specimens are expected in August 2004. Tests performed on the materials irradiated to lesser damage levels in the Halden BWR reactor may, however, give some insight into potential mechanisms for IASCC that is also relevant to PWRs. On the basis of these results, and studies on binary Ni-S and crack-tip microstructural characteristics of LWR core internal components reported in the literature, an initial IASCC model based on a crack-tip grain-boundary process that involves S has been proposed.

The resistance of Ni alloys to environmentally assisted cracking (EAC) in simulated LWR environments is being evaluated. Crack growth tests are being conducted to establish the effects of alloy chemistry, material heat treatment, cold work, temperature, load ratio, stress intensity, and DO level on the CGRs of Ni alloys. During this reporting period, CGR tests were conducted on an Alloy 182 SMA weld specimen and an Alloy 600 round-robin specimen in simulated PWR water at 320°C . The results for the Alloy 182 weld metal indicate that, in air, the cyclic CGRs are a factor of ≈ 5 higher than those for Alloy 600 under the same loading conditions. Also, some environmental enhancement was observed in PWR environment at $R = 0.7$ and very low loading frequencies. The CGRs obtained under constant load with periodic unload/reload have been compared with the available CGR data and trend lines from the literature. The CGR test was complemented by an extensive examination of the fracture surface conducted with the objective of correlating the test parameters to the resultant fracture modes.

A CGR test was conducted on an Alloy 600 round-robin specimen in a simulated PWR environment at 320°C according to the testing protocol agreed upon by the International Cooperative group on Environmentally Assisted Cracking. Under corrosion fatigue conditions, e.g., high load ratio and long rise times, the measured CGRs were higher than those for the alloy in air. The examination of the fracture surface revealed that the appearance of the crack front was U-shaped, implicating that the crack growth rates were significantly higher near the edge of the specimen than the center. This last observation is consistent with those made by other round-robin participants from France and Switzerland.

Initial results of orientation imaging microscopy (OIM) of the weld microstructure indicate that weld alloys contain relatively high proportions of cracking-susceptible random boundaries. In addition, OIM imaging revealed that the weld microstructure consists of clusters of grains sharing similar orientations. The possible implication of this finding is that weld alloys may contain a class of random boundaries that are more resistant to cracking when separating grains of similar orientations than different orientations.

Acknowledgments

The authors thank E. Listwan, T. M. Galvin, L. A. Knoblich, R. W. Clark, and J. Tezak for their contributions to the experimental effort. This work is sponsored by the Office of Nuclear Regulatory Research, U.S. Nuclear Regulatory Commission, under Job Code Y6388; Program Manager: William H. Cullen, Jr.; Tasks 2 and 3 Manager: Carol E. Moyer.

Intentionally Left Blank

Abbreviations

AAEM	Advanced Analytical Electron Microscopy
AES	Auger Electron Spectroscopy
ANL	Argonne National Laboratory
ASME	American Society of Mechanical Engineers
ASTM	American Society for Testing and materials
BWR	Boiling Water Reactor
CGR	Crack Growth Rate
CIR	Cooperative IASCC Research
CSLB	Coincident Site Lattice Boundary
CT	Compact Tension
CUF	Cumulative Usage Factor
CW	Cold Worked
DO	Dissolved Oxygen
EAC	Environmentally Assisted Cracking
ECP	Electrochemical Potential
EPR	Electrochemical Potentiodynamic Reactivation
FEG	field-emission-gun
GBE	Grain Boundary Engineered
GBO	Grain Boundary Optimized
GG	Grand Gulf
GTA	Gas Tungsten Arc
HAB	High Angle Boundary
HAZ	Heat Affected Zone
HWC	Hydrogen Water Chemistry
IAC	Irradiation Assisted Cracking
IASCC	Irradiation Assisted Stress Corrosion Cracking
IG	Intergranular
IHI	Ishikawajima–Harima Heavy Industries Co.
JOBB	Joint Owners Baffle Bolt
LAB	Low Angle Boundary
LWR	Light Water Reactor
MC	Metal Carbide

MHI	Mitsubishi Heavy Industries, Ltd.
MRP	Materials Reliability Program
NRC	Nuclear Regulatory Commission
NRR	Nuclear Reactor Regulation
NWC	Normal Water Chemistry
OIM	Orientation Imaging Microscopy
PWR	Pressurized Water Reactor
SA	Submerged Arc
SEM	Scanning Electron Microscopy
SCC	Stress Corrosion Cracking
SMA	Shielded Metal Arc
SS	Stainless Steel
SSRT	Slow Strain Rate Tensile
TG	Transgranular